Local dust plume analysis and classification using ground-based remote sensing and microphysical measurement acquired at Lhù'ààn Mân' (Kluane Lake), Yukon

Seyed Ali Sayedain*[1], Norman T. O'Neill[1], James King[2], Patrick L. Hayes[2], Daniel Bellamy[2], Richard Washington[3], Sebastian Engelstaedter[3], Andy Vicente-Luis[2], Jill Bachelder[2], Malo Bernhard[2]

[1]Centre d'Applications et de Recherches en Télédétection, Université de Sherbrooke, Sherbrooke, Canada (*seyed.ali.sayedain@usherbrooke.ca)

[2]Université de Montréal, Montréal, Canada

[3]University of Oxford, Oxford, United Kingdom

This presentation participates in OSPP

Outstanding Student & PhD candidate Presentation contest

INTRODUCTION

Local, drainage-flow dust events have recently been recognized as an important source of dust at high latitudes (Bullard et al., 2016). Local dust events in Canada are rarely monitored compared to other high-latitude countries. Low population density, limited numbers of meteorological stations, and problems with the use of remote sensing (RS) data in high-latitude regions have led to less frequent observations of local dust events in Canada (ibid).

The Lhù'ààn Mân' (the Southern Tutchone name for Kluane Lake) region is susceptible to frequent drainage-flow dust storms. We employed ground-based, passive and active RS techniques along with surface microphysical measurements to analyze the complementarity and redundancy of optical and microphysical retrievals relative to springtime coarse mode (CM) measurements of local dust at the Kluane Lake Research Station (KLRS). This included correlation analyses between ground-based CM aerosol optical depth (AOD) retrievals from AERONET AOD spectra, CM AODs derived from co-located Doppler lidar attenuated backscatter coefficient ($T^2\beta_c$) profiles and OPS (Optical Particle Sizer) surface measurements of CM particle-volume concentration.

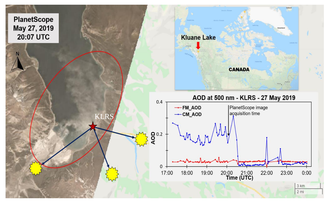

Figure 1: Lhù'ààn Mân' study area as seen in a PlanetScope satellite image. The North American context can be seen in the upper-right map and the typical variation of FM and CM AOD during the dust event seen in the PlanetScope image is shown in the graph in the bottom right. The yellow sun symbols show the sun-pointing, azimuth view direction of the CIMEL from 17:00 to 00:00.

RESEARCH SITE & DATA SETS

The Lhù'ààn Mân' (Kluane Lake) region, in the wake of the Slims River basin, is susceptible to frequent drainage-flow dust storms. Figure 1 shows a typical dust plume emanating from the basin. KLRS is an established observation site for the microphysical and meteorological analysis of high latitude dust emissions.

We employed a set of ground-based instruments including a CIMEL sunphotometer/sky radiometer, a Doppler Lidar, and an Optical Particle Sizer (OPS) at the KLRS to investigate the optical and microphysical properties of local dust events during May 2019 (the period of the most intense dust events). We employed Version 3.0 Level 1.0 AODs (high-frequency products of SDA$^+$) and Level 1.5 AERONET inversions (low-frequency products) to extract retrieval products that could be compared with the lidar and the KLRS OPS data sets.

The high frequency (11 s time bin) Doppler Lidar was resampled to the 1-minute CIMEL time bins. The fine mode (FM) AOD at the lidar wavelength is typically negligible (O'Neill et al., 2008): accordingly, the AODs retrieved by integrating the Doppler lidar vertical profiles are essentially CM AODs.

The KLRS OPS often provided important redundancy information when we sought to support the presence and nature of a given CM event. OPS data were resampled to the times of the SDA$^+$ retrievals for the correlation analysis.

ACRONYMS AND SYMBOLS

AERONET / AEROCAN Aerosol Robotic Network / Canadian network of CIMEL sunphotometer-sky radiometers
AOD Aerosol Optical Depth
CM Coarse Mode
DLH Dust Layer Height
FM Fine Mode
HLD High Latitude Dust
KLRS Kluane Lake Research Station
OPS Optical Particle Sizer
POI Period of Interest
PSD Particle Size Distribution
RS Remote Sensing
SDA Spectral Deconvolution Algorithm
β_c CM backscatter coefficient
r_{eff} Effective radius
R_{log} Correlation coefficient in log-log space ($\log\tau_c^\ell$ vs $\log\tau_c$ for example)
S_c^p Prescribed lidar ratio computed from Mie calculation
T Altitude dependent (one-way) transmission of a lidar pulse
τ_f FM AOD at 1548 nm (AERONET SDA$^+$ product)
τ_c CM AOD at 1548 nm (AERONET SDA$^+$ product)
$\tau_{c,inv}$ CM inversion AOD at 1548 nm (AERONET interpolated-inversion product)
τ_c^ℓ CM Lidar AOD at 1548 nm with integrating range of 0–DLH
τ_{β_c} Column-integrated CM backscatter coefficient (coarse mode backscatter optical depth)
$v_f(0)$ FM OPS particle-volume concentration
$v_c(0)$ CM OPS particle-volume concentration

METHODOLOGY

1. AERONET processing

The principal AERONET/AEROCAN product that we employed was the high frequency (1-minute averaging bin, 3-minute inter-sample gap) SDA$^+$ product (O'Neill et al., 2008) extrapolated to the Doppler SWIR wavelength of 1.548 µm. We label this ARONET-derived CM AOD as τ_c. Low frequency (nominally 1-hour inter-sample gap) AERONET inversion products (Dubovik & King, 2000) were also employed to compare their comprehensive microphysical and optical retrievals to SDA$^+$ and Lidar results.

2. Lidar processing

Lidar β_c profiles need to be vertically integrated in order to calculate Lidar AODs. A prescribed KLRS-derived lidar ratio for dust (S_c^p) and a prescribed lidar ratio for cloud (Chiang et al., 2002) were employed to calculate τ_c^ℓ for dust and cloud. If τ_{β_c} is defined as $\int \beta_{c,\sim}(z)\,dz$ (with $\beta_{c,\sim}$ being the approximated value of β_c extracted from the attenuated backscatter coefficient) then;

$$\tau_c^\ell \cong S_c^p \tau_{\beta_c}$$

where S_c^p is calculated using Mie computation (at the lidar wavelength of 1.548 µm) based on ground-based, particle size distribution (PSD) and dust speciation measurements and an assumption of (effective) particle sphericity.

3. OPS processing

The KLRS OPS PSD measurements of $dn/dlogD$ (particle number / unit volume of air / unit increment in logarithmic diameter) were converted to $dv/dlogD$ (particle-volume / unit volume of air / unit increment in logarithmic diameter) assuming spherical particles. We integrated the OPS PSDs over the CM radius range (bin-centers of 0.78 to 4.51 µm) to yield the CM particle-volume concentration ($v_c(0)$: the volume of all CM particles per unit volume of air).

4. Correlation analysis

Indicators of the optical significance and RS detectability of a dust event can be represented respectively by how dust-related τ_c^ℓ correlates with the KLRS OPS measurements of $v_{dust}(0)$ and how well τ_c correlates with dust-related τ_c^ℓ. In order to investigate the degree of coherency between the three different types of data, we analyzed their linear and logarithmic correlations.

5. Event classification

An automated dust classification scheme based on the coefficients of correlation between $v_{dust}(0)$, τ_c^ℓ and τ_c was developed to objectively identify local dust events. The first step in this process is to isolate apparent dust plumes in the vertical profiles of the lidar using a variable dust layer height (DLH). An estimate of lidar-derived dust optical depth (τ_{dust}^ℓ) can then be computed by vertical integrations of the β_c profiles (the approximate $\beta_{c,\sim}$ profiles to be exact) from the surface to the DLH.

We focused on two levels of correlation (in log-log space): the use of $R_{log}\left(\tau_{dust}^\ell \text{ vs } v_{dust}(0)\right)$ values as a means identifying and characterizing optically significant dust events and $R_{log}\left(\tau_c \text{ vs } \tau_{dust}^\ell\right)$ values to identify those events that could be remotely sensed by a ground- or satellite-based passive instrument. Figure 2 shows the flow-chart of the classification methodology. Our justification for the use of such a dust event flagging protocol is that correlation is a necessary (if insufficient) indicator of the presence of a dust event and that it is largely impervious to systematic instrumental issues (calibration issues for example).

REFERENCES

AboEl-Fetouh et al., 2020: Climatological-Scale Analysis of Intensive and Semi-intensive Aerosol Parameters Derived From AERONET Retrievals Over the Arctic, Journal of Geophysical Research: Atmospheres, 125(10), doi:10.1029/2019jd031569.

Bachelder et al., 2020: Chemical and microphysical properties of wind-blown dust near an actively retreating glacier in Yukon, Canada, Aerosol Science and Technology, 54(1), 2–20, doi: 10.1080/02786826.2019.1676394.

Baldo et al., 2020: Distinct chemical and mineralogical composition of Icelandic dust compared to northern African and Asian dust. Atmospheric Chemistry and Physics, 20(21), 13521–13539. https://doi.org/10.5194/acp-20-13521-2020.

Bullard et al., 2016: High latitude dust in the Earth system Reviews of Geophysics, Reviews of Geophysics, 54, 447–485, doi:10.1002/2016RG000518.

Chiang et al., 2002: Lidar ratio and depolarization ratio for cirrus clouds, Applied Optics, Vol. 41, Issue 30, Pp. 6470-6476, 41(30), 6470–6476, doi:10.1364/AO.41.006470, 2002.

Dubovik, O., & King, M. D., 2000: A flexible inversion algorithm for retrieval of aerosol optical properties from Sun and sky radiance measurements, Journal of Geophysical Research Atmospheres, 105(D16), 20673–20696, doi:10.1029/2000JD900282.

O'Neill et al., 2008: Coarse mode optical information retrievable using ultraviolet to short-wave infrared Sun photometry: Application to United Arab Emirates Unified Aerosol Experiment data, Journal of Geophysical Research Atmospheres, 113(5), 1–11, doi:10.1029/2007JD009052.

RESULTS

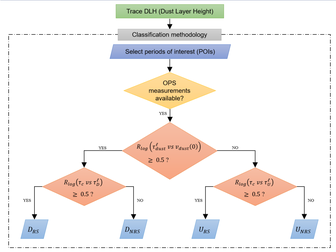

Figure 2: Flow-chart of the classification methodology. A "YES" from the second diamond-shaped decision box produces a "D" (dust) class. The next level of diamond-shaped decisions produces the subclasses of D_{RS} (dust that can be remotely sensed), D_{NRS} (dust that cannot be remotely sensed), U_{RS} (unclassified event that can be remotely sensed), U_{NRS} (unclassified event that cannot be remotely sensed).

The POI (period of interest) subclass results for the complete month of May 2019 are shown in Fig. 3 (b1 and b2) while the corresponding $R_{log}\left(\tau_{dust}^\ell \text{ vs } v_{dust}(0)\right)$ and $R_{log}\left(\tau_c \text{ vs } \tau_{(D \text{ or } U)}^\ell\right)$ values are shown in Fig. 3 (a1 and a2).

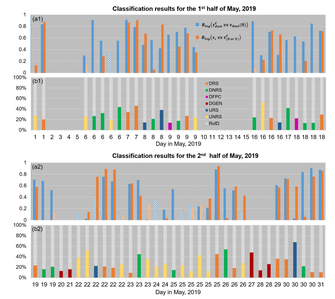

Figure 3: Correlation and classification results. The subclasses are represented as duty cycles (event duration as a percent of 24 h). The hatched R_{log} bars (coefficient of correlation in log-log space) represent negative values.

Figure 4 illustrates the D_{NRS} and D_{RS} subclasses (between the black- and red-dashed vertical lines). The lidar captures cloud and dust intrusions between the black vertical lines during which there are no SDA$^+$ retrievals. This is an example of largely legitimate cloud screening by triplet filtering of AODs prior to promotion to Level 1.0 AODs. The D_{RS} event is largely free of clouds while the τ_c and τ_{dust}^ℓ optical depths are moderately well correlated.

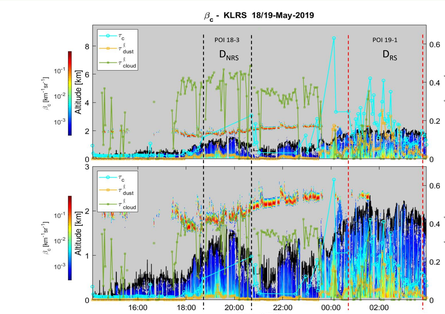

Figure 4: The D_{NRS} and D_{RS} subclass events of May 18 and the beginning of May 19, 2019.

Figure 5 is a plot of τ_U^ℓ vs $v_{dust}(0)$ for the U_{RS} subclass during May, 2019. The apparent bottoming out of all the point clusters in the scattergram is more about an apparently narrow spread driven by the densely packed log scale. The appearance of the POI 8-3 lidar profile (an obviously significant dust event which is, however, associated with quite weak τ_U^ℓ and τ_c values) and the temporal covariation of τ_U^ℓ and τ_c (associated with the orange points of Fig. 5) is strongly suggestive of an optically weak dust plume for which the covariation of τ_U^ℓ and τ_c is not some statistical artefact. This indicates that the physical significance of the columnar variability can occur within the (apparently narrow) spread of the point clusters in the scattergram.

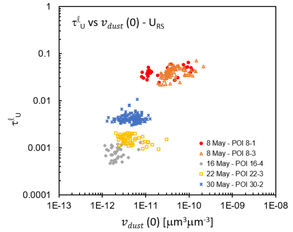

Figure 5: τ_U^ℓ vs $v_{dust}(0)$ for the U_{RS} subclass during May 2019.

The CM r_{eff} ($r_{eff,c}$) values for the whole month of May 2019 were calculated for all individual KLRS OPS PSDs that were part of class D POI events. A temporal plot of those individual $r_{eff,c}$ ($r_{eff,D}$) values can be seen in Fig. 6.

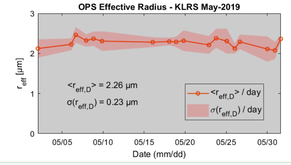

Figure 6: Variation of OPS-derived, class-D, r_{eff} values during the month of May 2019.

Clay, feldspar, and quartz minerals (in the order of decreasing mass fraction) are the major constituents of the PM10 dust particles in the Kluane Lake region (Bachelder et al, 2020). The method of Baldo et al. (2020) was employed, along with x-ray diffraction mineralogy applied to local dust samples, in order to compute a refractive index that would be representative of the Lhù'ààn Mân'region: $n = n_0(\pm\Delta n_0) - k_0(\pm\Delta k_0)\,i \;=\; 1.5371(\pm 0.0028) - 0.00075(\pm 0.00072)\,i$ at the lidar wavelength. A prescribed lidar ratio of 10.7 ± 0.9 sr was accordingly computed using a Mie code with the OPS-derived effective radius average and the derived refractive index as input.

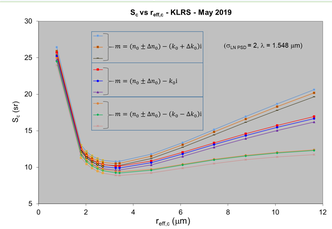

Figure 7: Mie (spherical-particle) computations of lidar ratio based on the mean and uncertainties of the refractive index (different colored curves) and $r_{eff,D}$ (orange circles: $\langle r_{eff,D}\rangle - 2\sigma(r_{eff,D})$ to $\langle r_{eff,D}\rangle + 2\sigma(r_{eff,D})$ in steps of $\sigma(r_{eff,D})$).

Individual ($\log\tau_{D_{RS}}$ *vs* $\log\tau_{RS}^\ell$) derived $S_{D_{RS}}$ values for each D_{RS} event were computed. The overall weighted result for the entire month of May 2019 was $\langle S_{D_{RS}}\rangle_\omega \pm \sigma_w(S_{D_{RS}}) = 28.0 \pm 3.3$ sr. The weighted mean, $\langle S_{D_{RS}}\rangle_\omega$, is roughly three times the S_D^p value. A measure of closer agreement with the S_D^p value was obtained by setting a higher standard on the $\log\tau_c^\ell$ vs $\log\tau_c$ regressions or the amplitude of the slant path lidar optical depth: $\langle S_{D_{RS}}\rangle_\omega$ values of 19.1 ± 2.3 sr and 20.3 ± 2.6 sr for $R_{log} > 0.9$ or slant path optical depth > 0.05 respectively. Given the persistence of this positive bias we sought to determine whether S_D^p could, in fact, be underestimated. A significant increase in its computed value can be obtained by assuming the general presence of larger, optically-significant dust particles in the plumes. Figure 7 indicates that an r_{eff} value ~ 11–12 µm and the higher value of the imaginary index of refraction ($k_0 +$ Δk_0) would push the S_D^p to values ~ 20 sr. The OPS cannot be employed to reject this hypothesis because of its limited upper radius of 4.5 µm.

Figure 8 shows the AERONET-inversion PSDs ($dV/dlnr$) for all retrievals during May 2019. One can observe bimodal CM peak positions near 1.3 and 5.0 / 6.6 µm. AboEl-Fetouh et al. (2020) ascribed the presence of a 1.3 µm component to the springtime incursion of Asian dust over six AERONET stations spread across the North American and European Arctic. The colored curve retrievals of Fig. 8 with the largest $\tau_{c,inv}$ represent the strongest local dust contributions (D_{RS} subclass). Four of these values are more dominated by the 5.0–6.6 µm peak while the other two are sufficiently weak to be dominated by a stronger 1.3 µm peak.

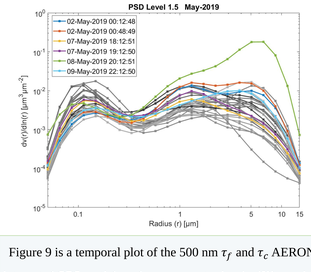

Figure 8: AERONET-inversion PSDs acquired during May 2019. The colored curves represent retrievals for the 6 largest $\tau_{c,inv}$ values, while the grey-colored curves include all other May 2019 retrievals (a mixture of D_{RS} and non D_{RS} subclasses).

Figure 9 is a temporal plot of the 500 nm τ_f and τ_c AERONET product, as well the FM-integrated OPS particle-volume concentration ($v_f(0)$) acquired during the D_{RS} POI. Correlations between the CIMEL-derived τ_f and OPS-derived $v_f(0)$ suggest that RS techniques can be employed to monitor FM dust (which is arguably a better indicator of the long-distance transport of HLD).

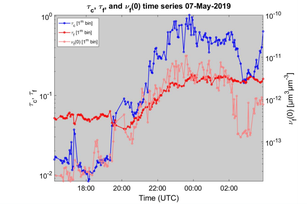

Figure 9: Temporal plot of τ_f and τ_c (500 nm) retrievals along with KLRS OPS surface particle-volume FM concentration $v_f(0)$ on May 7, 2019.

CONCLUSIONS

An automated and robust dust classification scheme involving CIMEL, lidar and OPS measurements was defined in order to objectively identify the presence and height of dust plumes as well as the potential for remotely sensing those dust plumes. The average OPS effective radius of class-D events as measured at the KLRS site during the month of May 2019 was estimated to be 2.26 ± 0.23 µm. X-ray diffraction mineralogy of local dust samples yielded their dust-species composition and thus enabled a calculation of the average refractive index at the 1.548 mm lidar wavelength ($n - ki \;=\; 1.5371 - 0.00075i$). A prescribed lidar ratio of 10.7 ± 0.9 sr was derived from Mie computations employing the OPS-derived effective radius average and the computed refractive index as input. The CIMEL-derived lidar ratio showed a positive bias that was anywhere from two to three times the prescribed ratio. The persistence of this positive bias led to a hypothesis that the prescribed value could be increased to the CIMEL-derived best estimate of 20 sr by hypothesizing the presence of optically significant dust particles at an effective radius of ~ 11–12 µm. This large-particle hypothesis is not incoherent with OPS measurements (such a particle size is greater than its 4.5 µm upper limit) and is coherent with the fact that the AERONET PSD retrievals showed a CM whose peak radius increased with increasing dust optical depth. The available inversions showed bimodal CM PSDs with (AERONET bin-center) peaks at radii ~ 1.3 µm and 5.0–6.6 µm and a tendency to be progressively more dominated by the latter peak as $\tau_{c,inv}$ increased. Evidence of a moderately strong FM dust optical depth (correlation with the FM OPS particle-volume concentration) indicated that such a component could be estimated using satellite-based remote sensing.

ACKNOWLEDGMENTS: Financial support was provided by the Canadian Mountain Network (CMN) and the Discovery Grant program of the Canadian National Sciences and Engineering Research Council (NSERC). Valuable in-kind support was provided respectively by the AEROCAN network of Environment and Climate Change Canada (ECCC) and the NASA AERONET network. Valuable AERONET processing advice was provided by Tom Eck and Sasha Smirnov of the AERONET team.